

# An intelligent colony optimization imaging method for composites health monitoring using ultrasonic guided wave

Jikang Yue, Xiaobin Hong<sup>\*</sup>, Bin Zhang

School of Mechanical and Automotive Engineering, South China University of Technology, Guangzhou 510641, People's Republic of China



## ARTICLE INFO

### Keywords:

Ultrasonic guided wave  
Composites health monitoring  
Intelligent damage imaging detection  
Scattering sources search

## ABSTRACT

Damage imaging technology based on ultrasonic guided wave can characterize and visualize structural damage. However, current imaging methods require high accuracy in wave packets information extraction, resulting in artifacts, large spots and false imaging. Therefore, an intelligent colony optimization imaging method is proposed to transform the damage imaging problem into the scattering sources search problem. The number of imaging trajectories through potential scattering sources is employed as the fitness function to assess the damage possibility in this individual. The fitness function is further implemented to particle swarm optimization algorithm for iterative search of actual scattering sources to find out the damage area with highest damage possibility. After the scattering sources search, the location of the damage can be identified through observing the distribution of the population. The experimental results illustrate that the proposed intelligent imaging method can accurately locate the crack damage of different lengths and delamination damage in composites, and the damage imaging effect is better than that of elliptic imaging.

## 1. Introduction

Composites have excellent properties in low mass, high specific strength, anticorrosion and antifatigue [1-3], and have been widely used in aerospace, marine, automotive and wind power [4-6]. During the long-term use of composites structures, various damages (such as holes, cracks, delamination) would occur, these damages will reduce the strength, integrity, safety and remaining useful life of composites and even cause huge economic losses. Therefore, it is of great theoretical significance and practical application value to conduct structure health monitoring of composites.

Ultrasonic guided wave, with the advantages of damage sensitivity, high efficiency, large detection range, and long propagation distance [7], has been widely used for nondestructive testing of plate structures such as composites, metals and other structures [8-12]. Especially, ultrasonic guided wave imaging method has become a research hotspot in the field of nondestructive testing and structural health monitoring in recent years because it can visually and clearly reflect the information of damage in the structure. The elliptic imaging method is a typical time-of-flight-based method by using ultrasonic guided wave sparse transducer arrays, and has been widely used in the visualization of plate structural damage. Xu et al. [13] developed a Lamb wave detection

technique based on the combination of sparse reconstruction and elliptic imaging method, which can achieve high damage localization resolution on composites. Qiu et al. [14] used the elliptic imaging method to detect the damage identification sub-regions divided by the piezoelectric sensor array, which significantly improved the detection efficiency of large-scale composite materials. Ren et al. [15] introduced a four-dimensional imaging algorithm based on Gaussian mixture model and ellipse imaging method, and successfully achieved defect imaging of aircraft composites under the condition of temperature change. Liu et al. [16] developed a probability imaging method of elliptical ring distribution, which uses the elliptical ring distribution function instead of the traditional weight distribution function, and uses the elliptical ring intersection area of different sensing channels to image and locate the damage. Zima et al. [17] proposed an improved damage elliptical probability imaging algorithm based on the binary of variable length linear cracks, which was simplified by assigning the damage pixels to binary, and conducted an experimental study on steel plates with variable length damage. Liu et al. [18] stated a velocity anisotropy imaging method to solve the problem that the damage is difficult to detect accurately due to velocity anisotropy of composites, but without imposing a threshold the imaging results have more artifacts. However, the positioning accuracy of the elliptic imaging method is greatly

\* Corresponding author.

E-mail address: [mexbhong@scut.edu.cn](mailto:mexbhong@scut.edu.cn) (X. Hong).

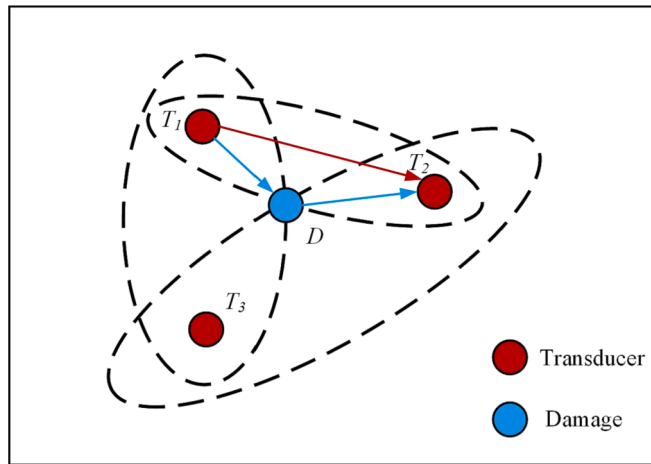


Fig. 1. Schematic diagram of elliptic imaging principle.

affected by the extracted wave packet information.

Recent years, intelligent optimization algorithms, such as, genetic algorithm (GA) and particle swarm optimization (PSO) [19], have raised the attention of researchers for the ability to solve practical engineering problems by simulating the colony behavior in natural or social environments. These algorithms have been widely used in nondestructive testing and structural health monitoring, including sensor array optimization [20–22], signal decomposition [23,24], damage identification, etc. Salmanpour et al. [25] utilized a GA to determine the optimal transducer array that could minimize the effect of faulty transducers and enhance damage localization. Chen et al. [26] used evolutionary strategy and K-means algorithm to realize intelligent damage imaging of aluminum plate. However, there are many input parameters in the algorithm, which has a great impact on damage imaging. Andhale et al. [27] proposed a Lamb wave-based damage localization method to detect damage in plain and riveted aluminum sheets. First, the asteroid algorithm is used to initially locate the damage location. Then, the damage is precisely searched by GA. Gomes et al. [28] used genetic algorithm and artificial neural network to identify and predict the delamination position of laminated composites. This method can not only identify the damage localization in structures, but also quantify the damage severity. Yan et al. [29] introduced an algorithm for damage detection and identification of composite materials based on wavelets and GA. The collected signals are processed by wavelet analysis, and the position of delamination damage is determined by GA. Therefore, the intelligent search algorithm is a promising path to avoid artifacts in traditional imaging methods and to intelligently determine damage information.

Elliptic imaging method can visualize the location and size of damage through mapping the wave packets information of the signal to each spatially discrete point of the component to be tested. However, the size and number of wave packets have affected the performance of elliptic imaging, resulting in artifacts, large spots, wrong imaging and other phenomena, which leads to the damage localization inaccurate. In this study, an intelligent colony optimization imaging method is proposed, which transforms the damage imaging problem into the scattering sources search problem. A fitness function of an intelligent imaging method is proposed, which is the number of imaging trajectories through potential scattering sources. The fitness function is applied to PSO algorithm for iterative search of actual scattering sources. After the scattering sources search, the location of the damage can be identified through observing the distribution of the population. The effectiveness and reliability of the proposed method are verified by crack damage of different lengths and delamination damage detection experiments in composites.

The remaining research content of this paper are as follows. Section 2 introduces the elliptic imaging principle and proposed intelligent

damage imaging method. Section 3 conducts crack damage of different lengths and delamination damage detection experiments in composites to verify the effectiveness the proposed method. Section 4 gives brief conclusion.

## 2. Theory and method

### 2.1. Elliptic imaging principle

When detecting the plate-like structure, at least three transducers are arranged on the tested plate as transmitter and receiver in turn. In this way, three groups of detection data can be obtained, that is, three elliptic trajectories with damage positions can be obtained. The intersection of the three elliptic trajectories, especially the place with the largest number of intersections, may be the location of the defect. Fig. 1 is the schematic diagram of the elliptic imaging algorithm. Among them,  $T_1$ ,  $T_2$  and  $T_3$  are transducers and  $D$  is damage. The working mode of the transducer is one send and one receive. When the signal sent by the transducer  $T_1$  encounters the damage  $D$ , scattering will occur, and the scattering signal continues to spread in all directions with the damage as the center, and then some scattering signals are received by the transducer  $T_2$ . Therefore, according to the scattering signal wave packet, we can extract the time  $t$  that ultrasonic wave is received by transducer  $T_2$  after it encounters damage  $D$  when transducer  $T_1$  is excited. If the group velocity  $c_g$  of guided wave in the medium is known, the sum of the distance from  $D$  to transducers  $T_1$  and  $T_2$  can be calculated as:

$$L = L_{T_1D} + L_{DT_2} = c_g t \quad (1)$$

According to the definition of elliptic, the damage  $D$  is located in the elliptic trajectory with the transducers  $T_1$  and  $T_2$  as the focus and the distance between the two focus is  $L$ .

According to the triangular geometric relationship, the time  $t$  for the Lamb wave to propagate from the transmitter  $T_i(x_t, y_t)$  to each discrete point  $P(x, y)$  in the plate and then to the receiver  $R_j(x_r, y_r)$  can be calculated by formula (2).

$$t_i(x, y) = \frac{\sqrt{(x_t - x)^2 + (y_t - y)^2} + \sqrt{(x_r - x)^2 + (y_r - y)^2}}{c_g} \quad (2)$$

The amplitude data of different transducer pairs obtained on each discrete point in the plate-like structure are added correspondingly, and the unique amplitude of each discrete point is obtained after fusion, as shown in formula (3).

$$I(x, y) = \sum_{i=1}^N S_i(t_i(x, y)) \quad (3)$$

where  $S_i$  represents the scattering signal of the  $i$ -th sensing path, that is, the difference between the detection signals when there is a defect in the plate and when there is no defect.  $S_i(t_i(x, y))$  represents the corresponding amplitude of the scattering signal at any discrete point in the plate at the time  $t_i(x, y)$ , and  $N$  is the number of sensing path. Multiple pairs of transducers in different positions are employed to form multiple elliptical trajectories, and their intersection is the location where the damage exists. The detection results of multiple sensing paths are fused to display the location or size of defect in the form of images, so as to realize the imaging detection of structural damage.

### 2.2. Proposed intelligent damage imaging method

Intelligent damage imaging method is designed through particle swarm optimization (PSO) algorithm combined with the elliptic imaging method. It utilizes PSO algorithm to search for scattering sources for damage localization. The individuals generated via initialization are potential scattering sources. The fitness function is designed according to the characteristics of elliptic imaging method. The damage

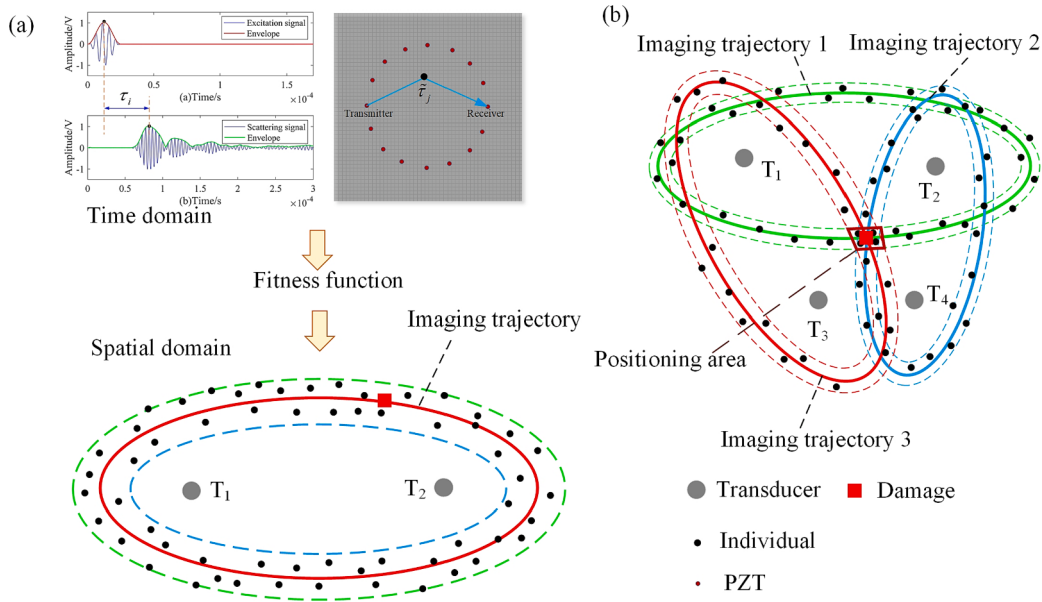


**Fig. 2.** The damage localization diagram of intelligent damage imaging method: (a) scattering signal is mapped from time domain to space domain, (b) individuals with multiple imaging trajectories for damage localization.

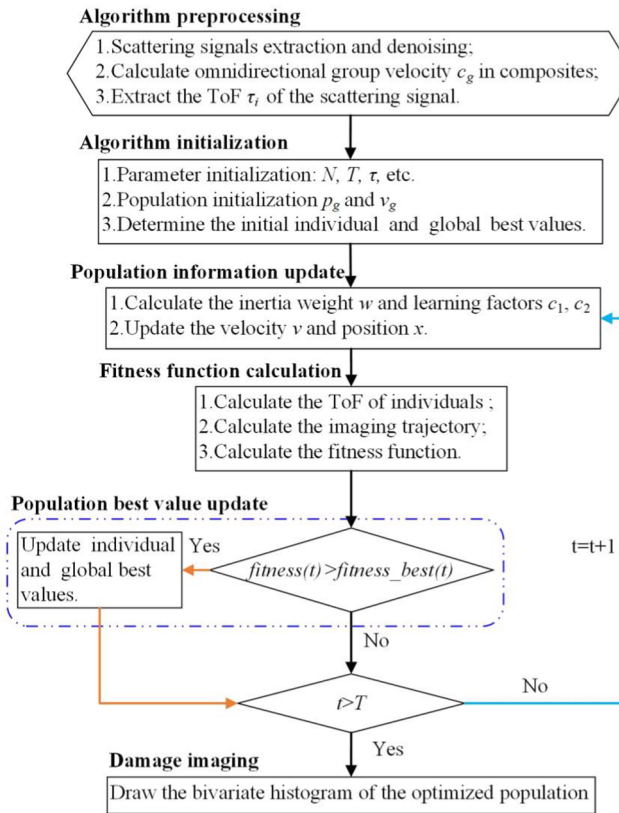


**Fig. 3.** Flow chart of intelligent colony optimization imaging method.

localization diagram of intelligent damage imaging method is shown in Fig. 2. The scattering signal of a sensing path in the time domain is mapped to the imaging trajectory in the space domain through the fitness function. A sensing path is formed into an imaging trajectory. The population will retain the individuals in the imaging trajectory through the fitness function, and at the same time, the retained individuals will obtain an imaging trajectory, as displayed in Fig. 2(a). The principle of damage location at the intersection of more than three imaging

trajectories is utilized. The more imaging trajectories an individual obtains, the more likely it is to be the damage location. Multiple individuals with the same number of imaging trajectories will form a positioning area, as illustrated in Fig. 2(b). Through PSO algorithm, individuals will continue to approach the individuals with the largest number of imaging trajectories, and eventually the entire population will converge to the location of damage.

Five sub-methods are processed for damage imaging, including algorithm preprocessing and initialization, population information update, population best value update and damage imaging analysis. The flow chart of the intelligent damage imaging method is shown in Fig. 3. The detail execution process of these sub-methods are as follows:

### 2.2.1. Algorithm preprocessing and initialization

The scattering signals are extracted via the difference between the detection signals with and without damage in the plate. The scattering signals are denoised by variational mode decomposition (VMD) denoising method. The omnidirectional group velocity  $c_g$  of composites is calculated. The time of flight (ToF) of the scattering signal is calculated using an envelope peak extraction algorithm. First, the Hilbert transform is performed on the scattering signal and the excitation signal. Then, the envelope is obtained by calculating the Hilbert transform modulus of the signal. Next, the time points  $\tau_i^s$  and  $\tau_i^e$  corresponding to the peaks in the envelope of the scattering signal and excitation signal are extracted, respectively. Finally, the absolute value of the difference between  $\tau_i^s$  and  $\tau_i^e$  is calculated to obtain  $\tau_i$ . The expression for  $\tau_i$  is as follows:

$$\tau_i^s = \operatorname{argmax} |HT(g_i^s(t))| \quad (4)$$

$$\tau_i^e = \operatorname{argmax} |HT(g_i^e(t))| \quad (5)$$

$$\tau_i = |\tau_i^s - \tau_i^e| \quad (6)$$

where  $HT$  represents Hilbert transform,  $g_i^s(t)$  and  $g_i^e(t)$  represent scattering signal and excitation signal of the  $i$ -th sensing path respectively.

The parameters of the intelligent damage imaging method are initialized, including population parameter range, population size  $N$ , maximum generation number  $T$  and time threshold control parameter  $\tau$ . In the PSO algorithm, the particle has two characteristics, that is, the

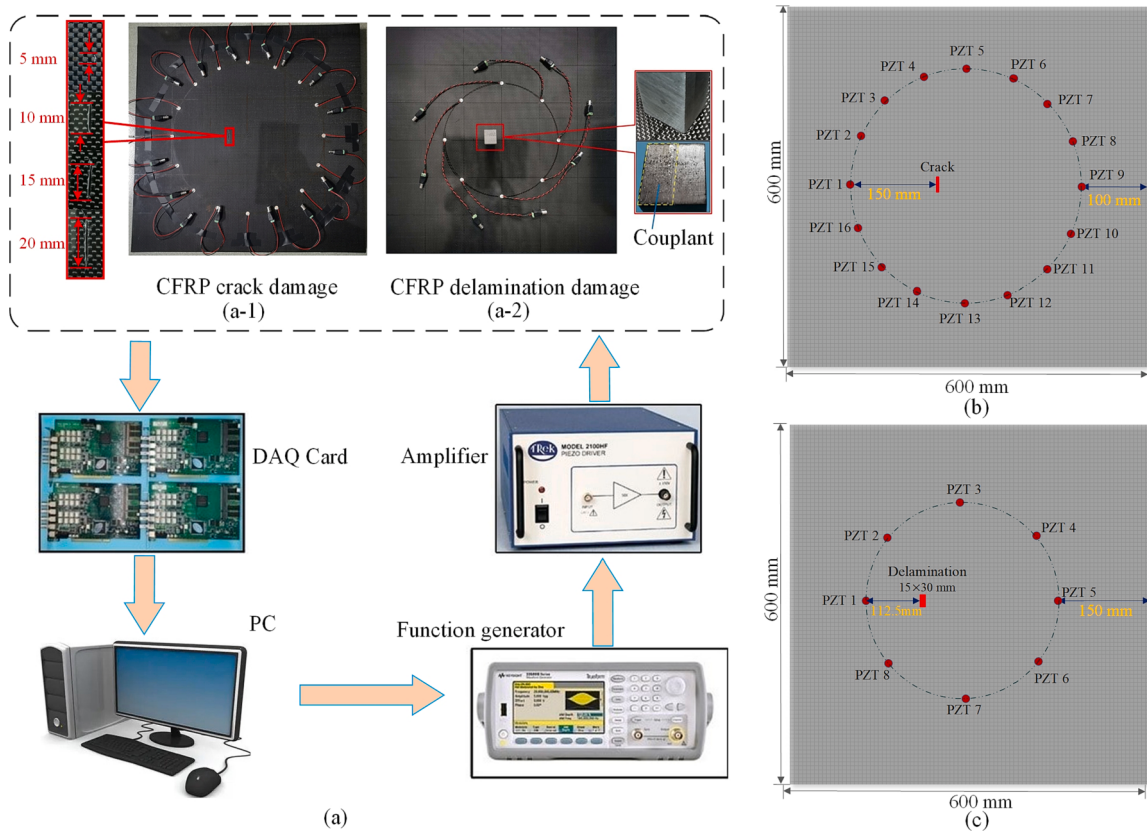


**Fig. 4.** Experimental setup for crack and delamination damage testing of CFRP: (a) equipment connection diagram, (b) crack damage and PZTs distribution in CFRP plate, and (c) delamination damage and PZTs distribution in CFRP plate.

**Table 1**

The properties of CFRP.

$\rho(\text{kg} \cdot \text{m}^{-3})$	$E_1(\text{GPa})$	$E_2(\text{GPa})$	$G_{12}(\text{GPa})$	$G_{23}(\text{GPa})$	$N_u$
1500	144.7	9.65	9.65	3.4	0.3

position  $p$  and the velocity  $v$ . The information of the particle itself is determined by  $p$  and  $v$ . At the beginning of the PSO, the  $p$  and  $v$  of particles are initialized randomly as follows:

$$\begin{cases} p_{g=0} = p_{\min} + (p_{\max} - p_{\min}) \times \text{rand}(1, d) \\ v_{g=0} = v_{\min} + (v_{\max} - v_{\min}) \times \text{rand}(1, d) \end{cases} \quad (7)$$

where  $\text{rand}$  represents the random number between 0 and 1,  $d$  represents the dimension and  $g = 0$  represents the 0th generation.

The individual optimal position  $p_{best}$ , the global optimal position  $g_{best}$ , the individual optimal fitness  $fitness\_p_{best}$  and the global optimal fitness  $fitness\_g_{best}$  are assigned initial values.

### 2.2.2. Population information update

In the search process, the particle updates its information according to the individual optimal value and the global optimal value. The particle information is updated as follows:

$$v^t = wv^{t-1} + c_1 r_1 (p_{best}^{t-1} - p^{t-1}) + c_2 r_2 (g_{best}^{t-1} - p^{t-1}) \quad (8)$$

$$p^t = p^{t-1} + v^t \quad (9)$$

where  $v^t$  and  $p^t$  represent the velocity and position of particle at the  $t$ -th generation, respectively,  $i \in [1, 2, \dots, N]$ ,  $d \in [1, 2, \dots, D]$ ,  $t \in [1, 2, \dots, T]$ .  $r_1$  and  $r_2$  are between [0,1] random numbers that obey uniform distribution.  $w$  is the inertia weight, which is employed to balance the global search capability of the early iterations and the local search capability of the later iterations, and its expression is as follows:

$$w = w_{\max} - (w_{\max} - w_{\min}) \frac{t}{t_{\max}} \quad (10)$$

where  $t$  is the current number of generations and  $t_{\max}$  is the maximum

**Table 2**

PZTs coordinates for CFRP crack detection (unit: mm).

PZT1 (-200,0)	PZT2 (-185,77)	PZT3 (-141,141)	PZT4 (-77,185)	PZT5 (0,200)	PZT6 (77,185)	PZT7 (141,141)	PZT8 (185,77)
PZT9 (200,0)	PZT10 (185,-77)	PZT11 (141,-141)	PZT12 (77,-185)	PZT13 (0,-200)	PZT14 (-77,-185)	PZT15 (-141,-141)	PZT16 (-185,-77)

**Table 3**

PZTs coordinates for CFRP delamination detection (unit: mm).

PZT1 (-150,0)	PZT2 (-106,106)	PZT3 (0,150)	PZT4 (106,106)	PZT5 (150,0)	PZT6 (106,-106)	PZT7 (0,-150)	PZT8 (-106,-106)

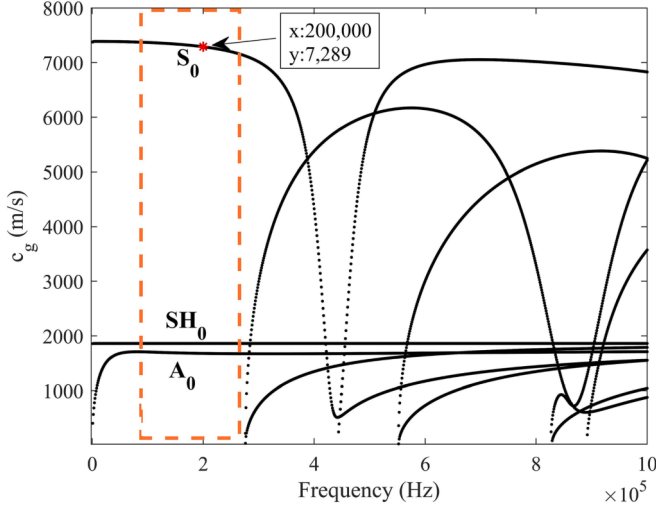


Fig. 5. The group velocity dispersion curve of CFRP.

number of generations.  $c_1$  and  $c_2$  are accelerating factors, which are applied to adjust the step size of particles flying toward the individual best point or the global best point. The specific formula of the typical dynamic asynchronous learning factor adjustment strategy is as follows:

$$\begin{cases} c_1 = c_{1,i} + \frac{c_{1,f} - c_{1,i}}{t_{\max}} t \\ c_2 = c_{2,i} + \frac{c_{2,f} - c_{2,i}}{t_{\max}} t \end{cases} \quad (11)$$

where,  $c_{1,i}$  and  $c_{2,i}$  denote the initial setting values of  $c_1$  and  $c_2$ , respectively.  $c_{1,f}$  and  $c_{2,f}$  represent the final setting values of  $c_1$  and  $c_2$ , respectively.

### 2.2.3. Fitness function calculation

The fitness function is employed to compare the advantages and disadvantages of the particles, and its velocity and position are constantly adjusted. The population is constantly approaching the global optimal solution of the problem to be optimized. The fitness function is the key to achieve damage imaging using the PSO algorithm. Therefore, the imaging trajectory is proposed based on the characteristics of the elliptic imaging method. The expression is as follows:

$$\varepsilon_{ij} = \begin{cases} 1, & |\tau_i - \tilde{\tau}_j| \leq \tau \\ 0, & |\tau_i - \tilde{\tau}_j| > \tau \end{cases} \quad (12)$$

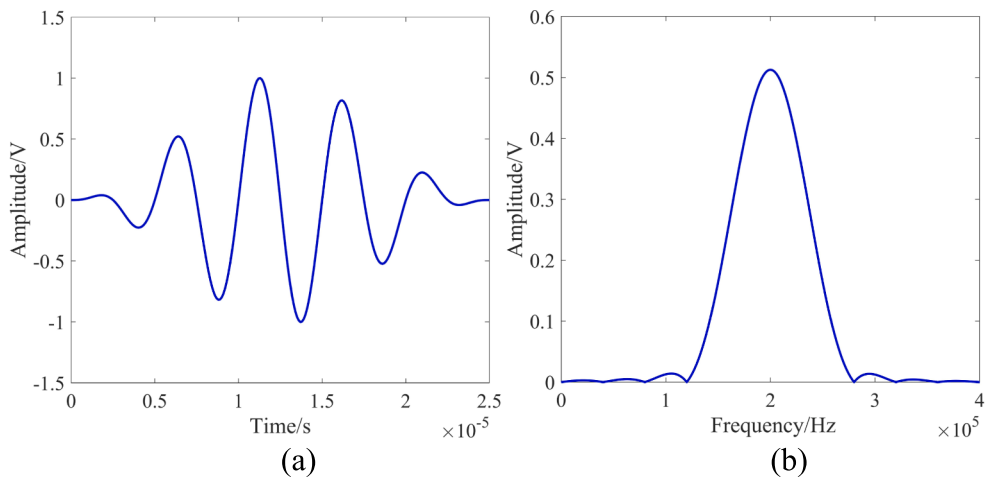


Fig. 6. A Hanning-windowed sine wave with 200 kHz, 5-peak: (a) temporal waveform of the excitation signal, (b) spectrum of the excitation signal.

where,  $\tau$  is the time threshold parameter, which controls the decay rate of the imaging trajectory,  $\tau_i$  is the ToF of the scattering signal for the  $i$ -th detection pair,  $\tilde{\tau}_j$  is the ToF of the  $j$ -th individual (potential scattering source). The details of the  $\tilde{\tau}_j$  are as follows:

$$\tilde{\tau}_j = \frac{\sqrt{(x_j - x_t)^2 + (y_j - y_t)^2}}{c_g(\alpha_t)} + \frac{\sqrt{(x_j - x_r)^2 + (y_j - y_r)^2}}{c_g(\alpha_r)} \quad (13)$$

where,  $(x_j, y_j)$ ,  $(x_t, y_t)$  and  $(x_r, y_r)$  are the coordinate of the individual, transmitter and receiver, respectively. Because the composites are anisotropic, the group velocity in all directions is calculated.  $c_g(\alpha)$  is the group velocity when the guided wave propagation angle is  $\alpha$ .  $\alpha_t$  is the propagation angle from the transmitter to the individual, and  $\alpha_r$  is the propagation angle from the individual to the receiver.

$\varepsilon_{ij}$  being 0 means that the  $i$ -th imaging trajectory does not pass through the  $j$ -th individual.  $\varepsilon_{ij}$  being 1 means that the  $i$ -th imaging trajectory passes through the  $j$ -th individual. The fitness function is obtained by summing the imaging trajectories of the individuals, and its expression is as follows:

$$\text{fitness} = \sum_{i=1}^N \varepsilon_{ij} \quad (14)$$

where  $N$  is the maximum number of sensing paths.

### 2.2.4. Population best value update

In the iterative process, the population updates the individual best value and the global best value via comparing the fitness function. If the current generation individual fitness is higher than the individual best fitness, the individual best fitness is replaced by the current generation individual fitness. And the individual best position is replaced with the current generation individual position. If the individual best fitness is higher than the global best fitness, the global best fitness is replaced by the individual best fitness. And the global best position is replaced with the individual best position. As shown in the following formula:

$$\begin{aligned} &\text{if } \text{fitness}(t) > \text{fitness\_pbest}(t) \\ &\text{then } \text{fitness\_pbest}(t) = \text{fitness}(t) \\ &\quad p_{\text{best}}(t) = p(t) \\ &\text{if } \text{fitness\_pbest}(t) > \text{fitness\_gbest} \\ &\text{then } \text{fitness\_gbest} = \text{fitness\_pbest}(t) \\ &\quad g_{\text{best}} = p_{\text{best}}(t) \end{aligned} \quad (15)$$

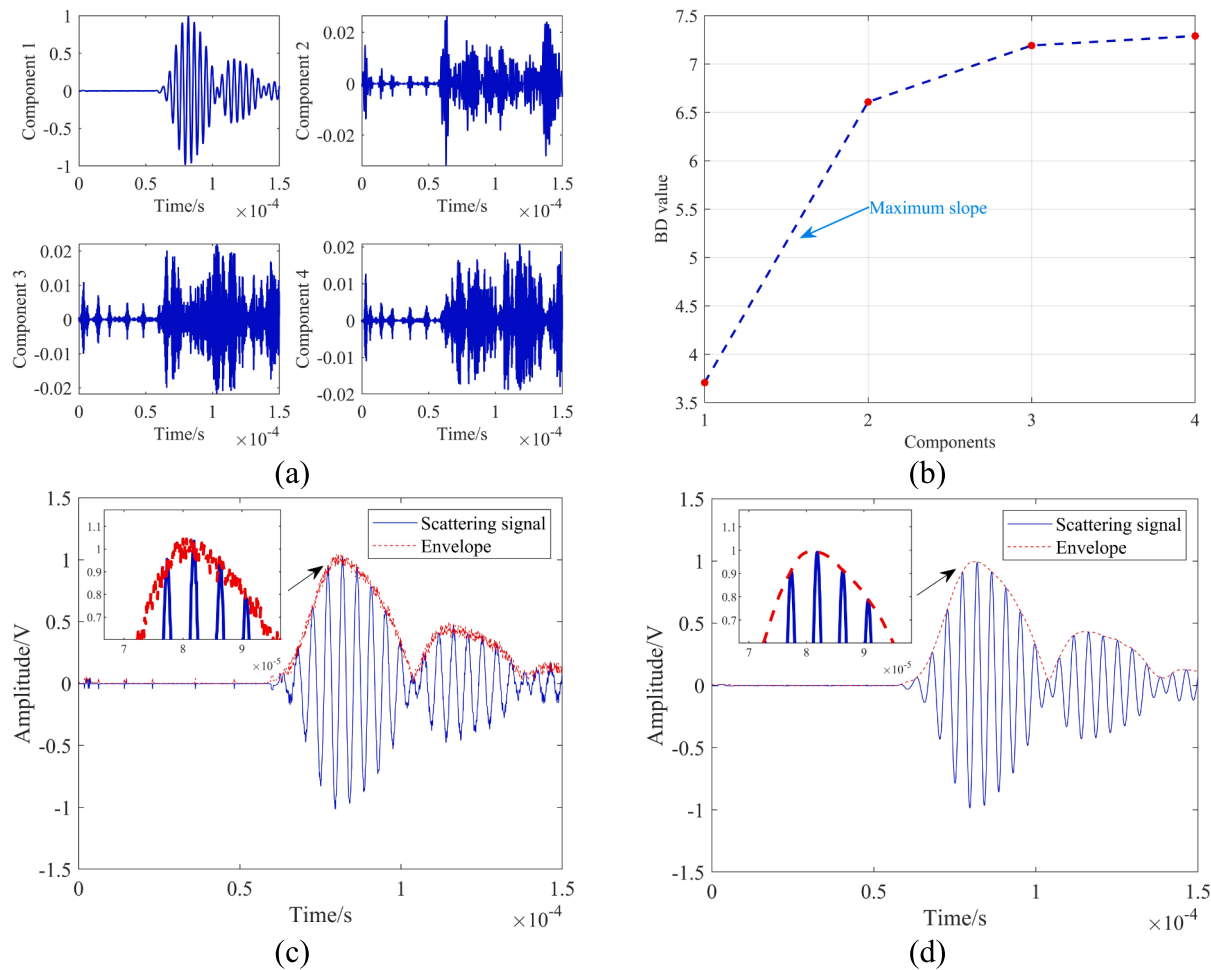


**Fig. 7.** The denoising process of the scattering signal: (a) components of the scattering signal, (b) change curve of Bhattacharyya distance, (c) raw scattering signal, and (d) denoised scattering signal.

### 2.2.5. Damage imaging

Whether the algorithm satisfies the termination condition at the current iteration is judged. When the number of generations does not meet the max number of iterations  $T$ , this step will return to the population information update and continue to execute the cycle. When the number of generations meets the maximum number of generations  $T$ , the iterative process of the algorithm ends. The fitness function curve and the optimized population are output. The optimized population is plotted with MATLAB function “histogram2”. Then, the damage position is determined by evaluating the pixel value of the bivariate histogram, and the location with high pixel value is the damage position.

## 3. Experimental validation and discussions

### 3.1. Experimental setup

The effectiveness of the proposed intelligent damage imaging method was validated through the detection of crack and delamination damage in carbon fiber reinforced plastic (CFRP). The experimental setup for CFRP damage detection is illustrated in Fig. 4. The main parts of the experiment include CFRP, an amplifier, an arbitrary function generator, a 16-channel data acquisition card and PC. The CFRP plate is T300 type. The geometric size of the plate is  $600\text{mm} \times 600\text{mm} \times 3\text{mm}$ . The number of layers is 15, the layup form is  $[0/90/\dots/0]$ , and every ply thickness of CFRP is 0.2 mm. The properties of CFRP are presented in Table 1. The piezoelectric lead zirconate titanate (PZT) is used as the ultrasonic transducer. CFRP damage detection experiment is divided

into two cases. In case A, different lengths of crack damage of 5 mm, 10 mm, 15 mm and 20 mm are set on CFRP. The connection diagram of crack damage detection is shown in Fig. 4(a-1). The long strips in the amplified part in the figure represent crack damage of different lengths, with sharp boundaries and direction. The crack damage and PZTs distribution are shown in Fig. 4(b), and a total of 16 PZTs are set to form a circular array. The PZTs are numbered clockwise as PZT1-PZT16. The crack is located 150 mm to the right of PZT1. In case B, half of the surface area of the bottom of the mass block is pressed on the surface of the CFRP structure by a coupling agent (Dow Corning HVG, Midland, MI, USA) to form two mutually separated but not completely separated surfaces. This process is similar to contact delamination damage, which can simulate the delamination damage between the surface layer and the sub-surface layer to a certain extent. The simulated delamination damage size was  $15 \times 30$  mm. Because the mass block is attached to the CFRP surface through a coupling agent, the position of the mass block can be adjusted according to experimental requirements. The connection diagram of CFRP structure delamination damage detection is shown in Fig. 4(a-2). The delamination damage and PZTs distribution are shown in Fig. 4(c). A total of 8 PZTs are set to form a circular array. The PZTs are numbered clockwise as PZT1-PZT8. The delamination damage location is 112.5 mm to the right of PZT1. The coordinate system is established with the center of the CFRP plate as the origin of coordinates. The coordinates of PZTs in Fig. 4 (b) and (c) are rounded to single digits, as shown in Table 2 and Table 3. In this paper, a one transmit multiple receive method is used, where only one PZT is excited at a time and the remaining PZTs collect signals simultaneously. In this

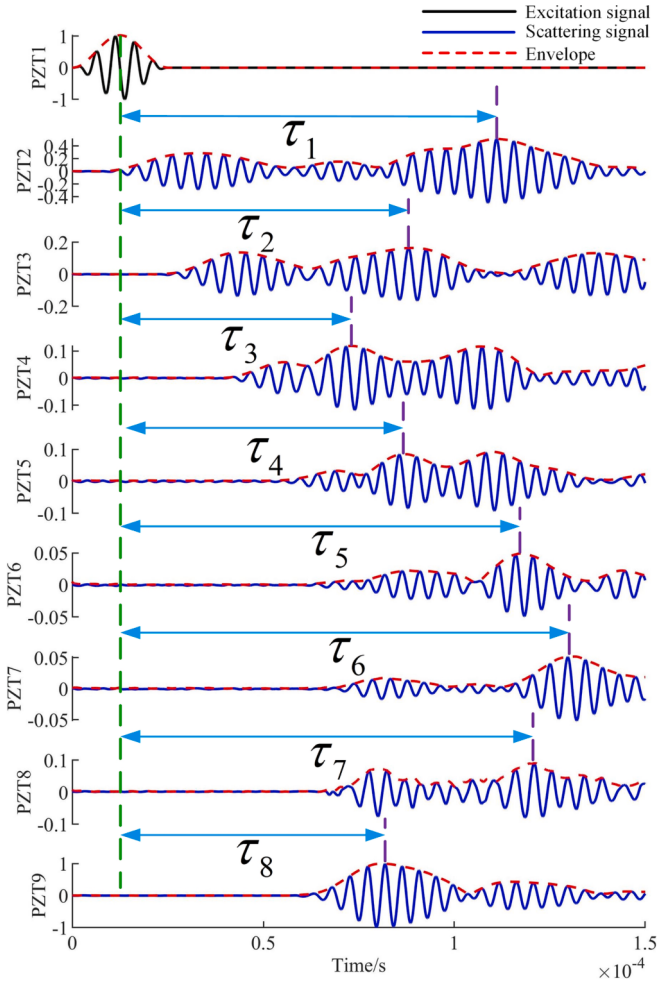
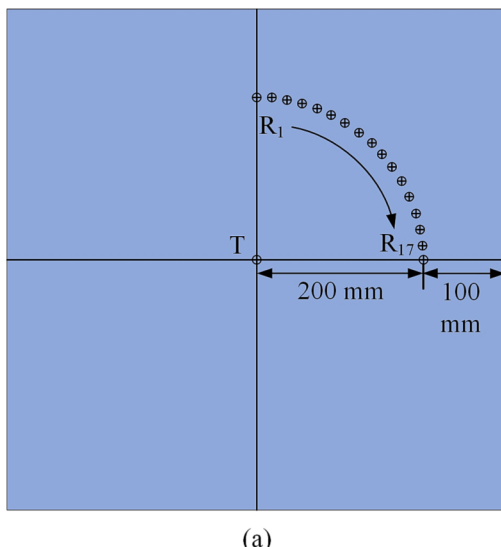


**Fig. 8.** The ToF extraction process of scattering signals received from PZT2 to 9, when PZT1 is excited.

way, all PZTs are cycled. For crack damage detection with 16 PZTs, a total of 240 sets of signals are collected, and for delamination damage detection with 8 PZTs, a total of 56 sets of signals are collected.

The dispersion curve of the CFRP structure is calculated using the



GUIGUW software suggested in Bocchini et al [30]. The group velocity dispersion curve of CFRP is displayed in Fig. 5. It can be observed from the graph that in the area of 60 kHz to 300 kHz, there are few guided wave modes and the group velocity of the guided waves in each mode is relatively stable and has almost no dispersion. Therefore, a Hanning-windowed sine wave with 200 kHz, 5-peak is chosen as the excitation signal. The following equation is illustrated:

$$I(t) = \left[ H(t) - H\left(\frac{N}{f_c}\right) \right] \left[ 1 - \cos\left(\frac{2\pi f_c t}{N}\right) \right] \sin(2\pi f_c t) \quad (16)$$

where  $f_c$  is the central excitation frequency of the guided wave.  $H(t)$  is the Heaviside step function.  $N$  is the number of crests of the sine-modulated signal. The temporal waveform and the spectrum of the excitation signal are shown in Fig. 6.

### 3.2. Signal preprocessing

The scattering signals before 150  $\mu$ s are extracted for damage detection. The scattering signals are denoised by VMD denoising method [31], in which the penalty factor and the number of decomposition layers are set to 2000 and 4, respectively. The denoising process of the scattering signal of 1T-9R (represents PZT1 transmitter and PZT9 receiver) by VMD is shown in Fig. 7. Firstly, the scattering signal is decomposed through VMD to obtain 4 components, as illustrated in Fig. 7(a). The result show that component 1 is the required signal, while the other components are noise. Then, the method in literature [31] is used to identify the effective component. The change curve of Bhattacharyya distance (BD) between the component signals and the raw scattering signal is presented in Fig. 7(b). The maximum slope of the BD value curve is between component 1 and 2, so component 1 is identified as the effective component. Finally, the de-noised scattering signal is obtained by reconstructing the effective component. The scattering signal before and after denoising are displayed in Fig. 7 (c) and (d). Through the comparison of local amplified images, it can be seen that there are a large number of “burrs” in the envelope of scattering signal without denoising, and the peak time cannot be accurately obtained. The envelope of the denoised scattering signal is smoother and the peak time can be accurately obtained. The scattering signals of all sensing paths are processed by the above denoising method.

The ToF of scattering signals of all sensing paths is extracted. When PZT1 is the transmitter, PZT2 to 9 are the receivers as an example. The ToF extraction process of the scattering signal is shown in Fig. 8. Hilbert

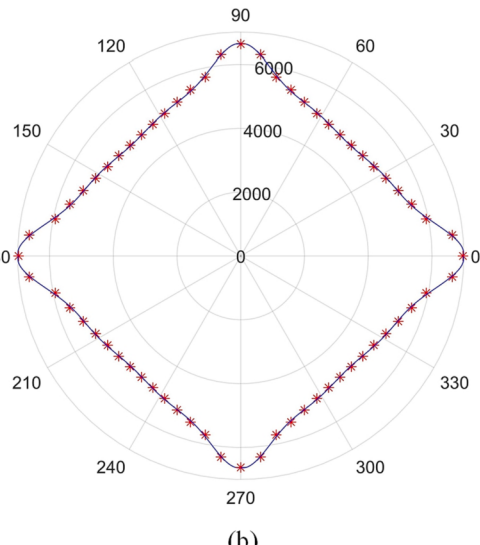


**Fig. 9.** Calculation of omnidirectional guided wave velocities of CFRP: (a) the distribution of the PZTs, (b) fitting results of the guided wave velocities of CFRP in polar coordinates.

**Table 4**

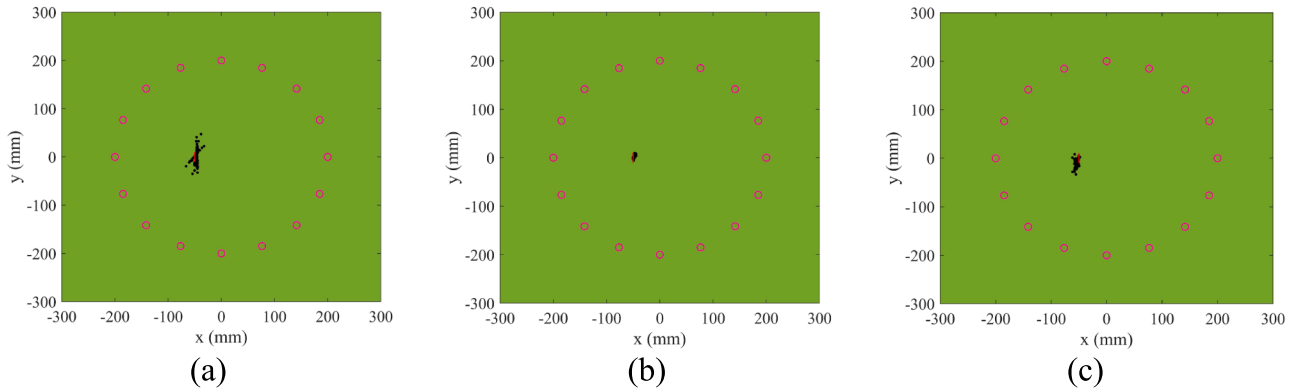
Calculation results of guided wave velocities of receivers.

PZT No. V (m/s)	R <sub>1</sub> 6625.4	R <sub>2</sub> 6310.6	R <sub>3</sub> 5758.2	R <sub>4</sub> 5397.6	R <sub>5</sub> 5209.4	R <sub>6</sub> 5087.9	R <sub>7</sub> 4980.7	R <sub>8</sub> 4900.3	R <sub>9</sub> 4882.2
PZT No. V(m/s)	R <sub>10</sub> 4940.9	R <sub>11</sub> 5053.8	R <sub>12</sub> 5184.5	R <sub>13</sub> 5330.0	R <sub>14</sub> 5560.4	R <sub>15</sub> 5995.0	R <sub>16</sub> 6637.6	R <sub>17</sub> 6973.7	

**Table 5**

Guided wave velocities differences of receivers.

PZT No. R <sub>diff</sub>	R <sub>1</sub> 4.99%	R <sub>2</sub> 9.51%	R <sub>3</sub> 17.43%	R <sub>4</sub> 22.60%	R <sub>5</sub> 25.30%	R <sub>6</sub> 27.04%	R <sub>7</sub> 28.58%	R <sub>8</sub> 29.73%	R <sub>9</sub> 29.99%
PZT No. R <sub>diff</sub>	R <sub>10</sub> 29.15%	R <sub>11</sub> 27.53%	R <sub>12</sub> 25.66%	R <sub>13</sub> 23.57%	R <sub>14</sub> 20.27%	R <sub>15</sub> 14.03%	R <sub>16</sub> 4.82%	R <sub>17</sub> 0%	

**Fig. 10.** PSOIIM positioning results for 20 mm crack with different time thresholds: (a) positioning result for  $\tau = 3 \mu\text{s}$ , (b) positioning result for  $\tau = 4 \mu\text{s}$ , and (c) positioning result for  $\tau = 5 \mu\text{s}$ .

transform is performed on the excitation signal and the scattering signals, respectively. The red dotted line in the figure is the envelope of the excitation signal and the scattering signals. The green dotted line and the purple dotted line represent the time corresponding to the envelope peak of the excitation signal and the scattering signals, respectively. The time difference between the green dotted line and the purple dotted line is ToF of the scattering signals.

Multiple receiving points are set up via the transducer array, and the guided wave velocity at multiple angles of the anisotropic CFRP structure can be obtained. A transmitter is arranged in the center of the CFRP structure. The seventeen receivers are installed in the first quadrant and are uniformly arranged on a 1/4 circle at a distance of 200 mm from the transmitter, as shown in Fig. 9(a). The multi-angle guided wave received signals of anisotropic CFRP structure are obtained. The ToFs of the received signals are obtained by the envelope peak extraction algorithm. The distance between each receiver and transmitter is calculated. Then, the guided wave velocities in all direction of CFRP structure are computed from the velocity formula. The calculation outcomes are listed in Table 4. Due to the symmetry of the four quadrants, the multi-angle guided wave velocities are obtained by polynomial fitting. The fitted results are displayed in the form of polar coordinates to intuitively show the difference of velocity in different directions, as demonstrated in Fig. 9(b). From the figure, it is observed that the velocities of the anisotropic CFRP structure with the layup direction [0/90/<sub>alternative</sub>.../0]<sub>15</sub> in all directions displays a diamond-shaped. In order to conduct quantitative analysis of velocity varies in different directions, guided wave velocity in the 0° direction is taken as the reference, and the difference of wave velocity in different directions is quantified according to equation (17):

$$R_{\text{diff}} = \frac{|c_g^{R_i} - \max(C_g)|}{\max(C_g)} \times 100\% \quad (17)$$

where  $c_g^{R_i}$  is the guided wave velocity corresponding to receiver  $R_i$  and  $C_g$  is the set of guided wave velocities in Table 4.

The guided wave velocity differences corresponding to each receiver are shown in Table 5. It can be seen that the of guided wave velocities in different directions have significant differences. Since the guided wave velocity in the direction of 0° is the reference, the velocity difference is 0, and the maximum wave velocity observed is 6973.7 m/s. Receiver R<sub>1</sub> in the 90° direction and this position also has an angle of 0° with the layup direction and the velocity difference is 4.99%. R<sub>2</sub> and R<sub>16</sub> have a small angle with the layup direction, and the velocity difference is 9.51% and 4.82%, respectively. However, the guided wave velocity differences of other receivers such as R<sub>3</sub>-R<sub>15</sub> are also increasing due to the increasing angle between them and the layup direction, which are more than 10%. The guided wave velocity differences of receivers such as R<sub>4</sub>-R<sub>14</sub> are more than 20%. The velocity difference of receiver R<sub>9</sub> in the 45° direction (with the largest angle from the layup direction) reached a maximum of 29.99%, and the observed minimum wave velocity is 4882.2 m/s. In fact, when the guided wave propagates along the 90° direction, the angle between the spreading direction and the layup direction is also 0°. However, since the layup directions of the upper and lower surfaces of the anisotropic CFRP structure are both 0°, the velocity of the guided wave propagation along the 0° direction is slightly greater than that along the 90° direction.

### 3.3. Case A: Crack damage detection

In this section, the application performance of the proposed algorithm for crack detection is evaluated. The parameters of the PSOIIM are initialized. The population size  $N$  has to balance computational efficiency and search damage accuracy, so the population size is set to 1000. The maximum iteration number  $T$  should balance the computational efficiency and the number of iterations when the population completes

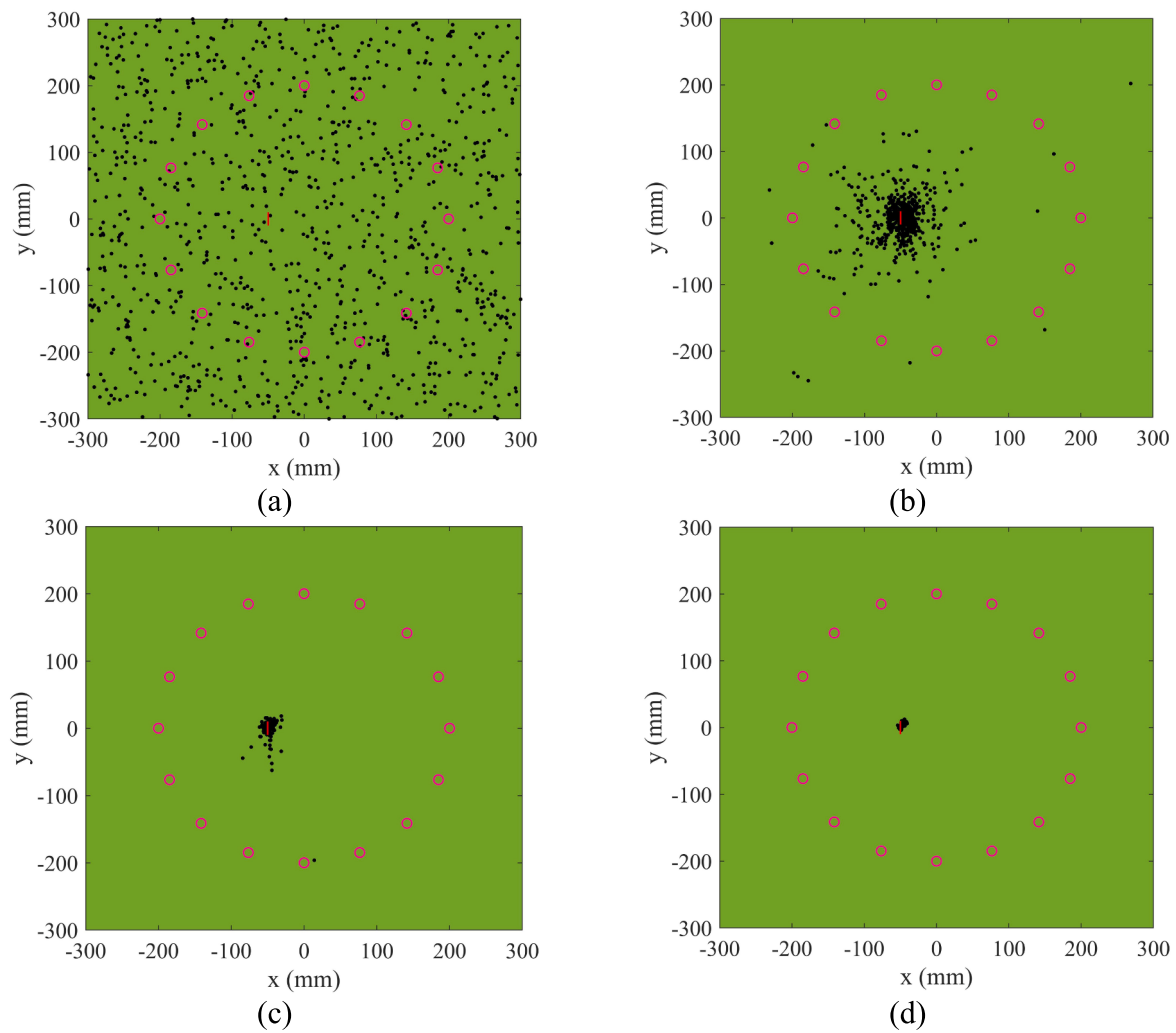


**Fig. 11.** The evolution process of particle swarm search damage with increasing number of generations: (a) Random distribution of particle swarm at the 0th generation, (b) particle swarm searches for damage result at the 25th generation, (c) particle swarm searches for damage result at the 50th generation, and (d) particle swarm searches for damage result at the 75th generation.

convergence. Although previous generations of PSO have searched for the optimal individual location and the fitness function has completed convergence, the entire population needs to converge towards the optimal individual location during the iteration process. After several different iteration times verification, the population convergence is completed when the maximum iteration number  $T$  is set to 100. The coordinate system is established with the center of the plate as the coordinate origin, and the coordinate range in both the  $x$  direction and the  $y$  direction is [-300,300], so the parameter range of position  $p$  is given as [-300,300]. Because of  $v_{max} = k \cdot p_{max}$ ,  $v_{min} = -v_{max}$ ,  $0.1 \leq k \leq 1$ ,  $k$  is set as 0.1 in this experiment, so the parameter range of velocity  $v$  is given as [-30, 30]. The time threshold  $\tau$  is a parameter that affects the location accuracy. For example, PSOIIM with different time thresholds locates a 20 mm crack, as shown in Fig. 10. The optimal location accuracy can be achieved by setting the time threshold  $\tau$  as 4  $\mu$ s.

Damage is taken as food source by particle swarm, which is gradually gathered to damage under the driving of survival law. The evolution process of particle swarm search damage with increasing number of generations is shown in Fig. 11. In the figure, the red solid line represents crack damage, the pink circles represent PZTs, and the black dots represent individuals. The particle swarm is randomly generated at the 0th generation. It is clear from Fig. 11(a) that the individuals are randomly distributed. The search results of PSO at the 25th generation are presented in Fig. 11(b). Under the guidance of the optimal

individual, the particle swarm gradually converges to the damage by comparing the fitness value. At the 50th generation, as displayed in Fig. 11(c), the search range of the particle swarm is further narrowed and further focused on the location of the damage. In the 75th generation, as shown in Fig. 11(d), most of the particle swarm clustered at the damage location, and the search was almost completed.

In order to verify the effectiveness of the proposed method, a total of 5 mm, 10 mm, 15 mm and 20 mm crack damage are set for experiments in this section. The PSOIIM localization results for different crack damages in CFRP structures are shown in Fig. 12. The results in the diagram show that PSOIIM can accurately localize crack damages of different lengths.

The convergence curves of the fitness function for PSOIIM to locate cracks with different lengths are illustrated in Fig. 13(a). The fitness function of PSOIIM locating 5 mm crack completed convergence in the 2th generation, in other words, some a certain best individual searched for the damage location in the 2th generation. The entire population is converged to the damage location in subsequent iterations. The best fitness value is 87, in other words, the maximum number of imaging trajectories through the damage location is 87. The fitness functions of 10 mm, 15 mm and 20 mm cracks located by PSOIIM converged in the 3th, 2th and 18th generation, respectively, and the maximum number of imaging trajectories through the damage location were 90, 97 and 80, respectively. In general, PSOIIM has a faster search speed for locating 5

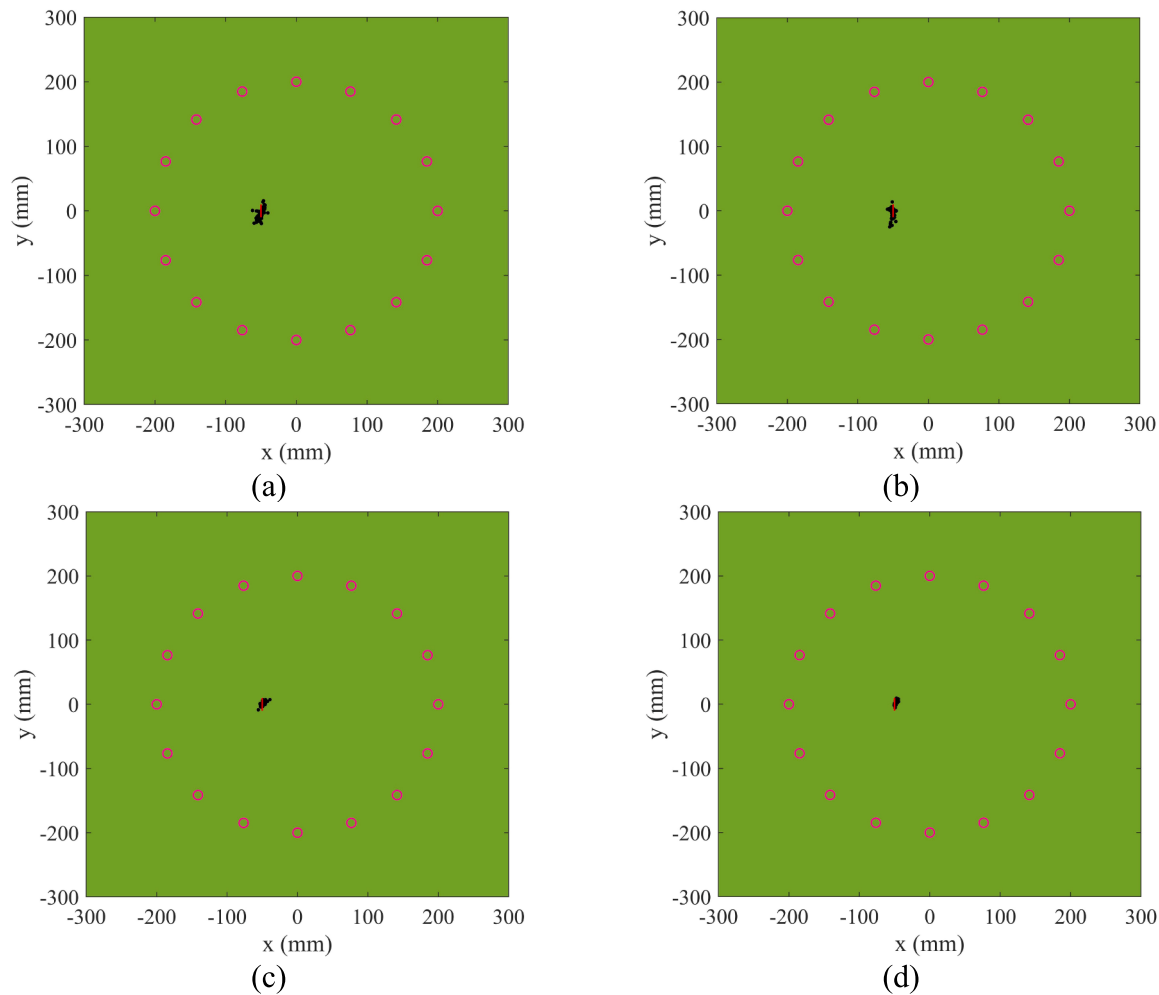


**Fig. 12.** PSOIIM localization results for crack damage with different length: (a) 5 mm crack localization result, (b) 10 mm crack localization result, (c) 15 mm crack localization result, and (d) 20 mm crack localization result.

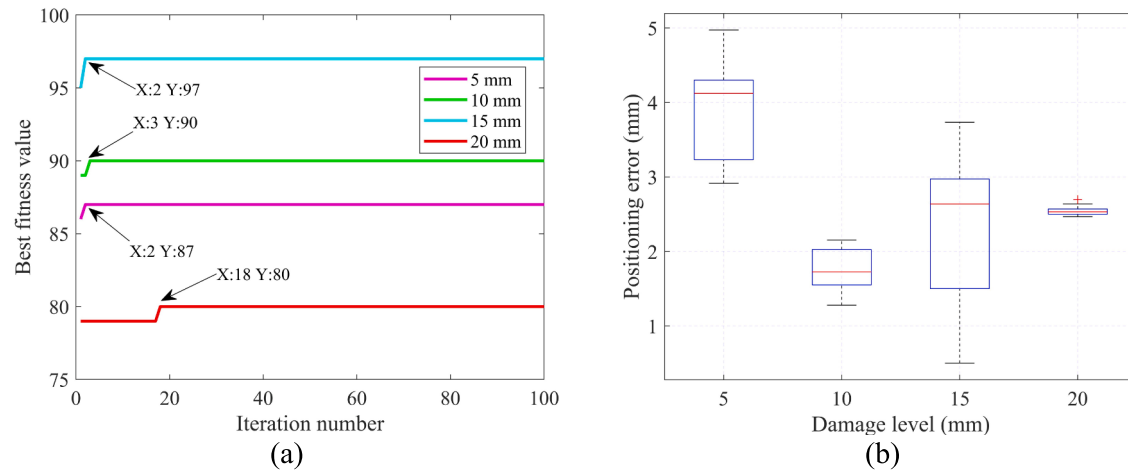


**Fig. 13.** (a) The convergence curves of the fitness function for PSOIIM to locate cracks with different lengths, (b) positioning error boxplots of PSOIIM locating cracks with different lengths.

mm, 10 mm and 15 mm cracks, but a slower search speed for locating 20 mm cracks.

In order to verify the robustness of PSOIIM, PSOIIM is run 10 times respectively when locating different crack damages, and the positioning errors (the distance between the optimal individual position and the actual damage position) are recorded and boxplots are drawn as shown

in Fig. 13 (b). In the figure, “+” represents outliers, the blue rectangle represents the box, and the red line represents the median line. As can be viewed from the graph, the positioning error of 5 mm crack is on the whole high, and that of 10 mm crack is on the whole low. PSOIIM has the worst robustness for locating 15 mm crack, and PSOIIM has the strongest robustness for locating 20 mm crack. In general, PSOIIM has different

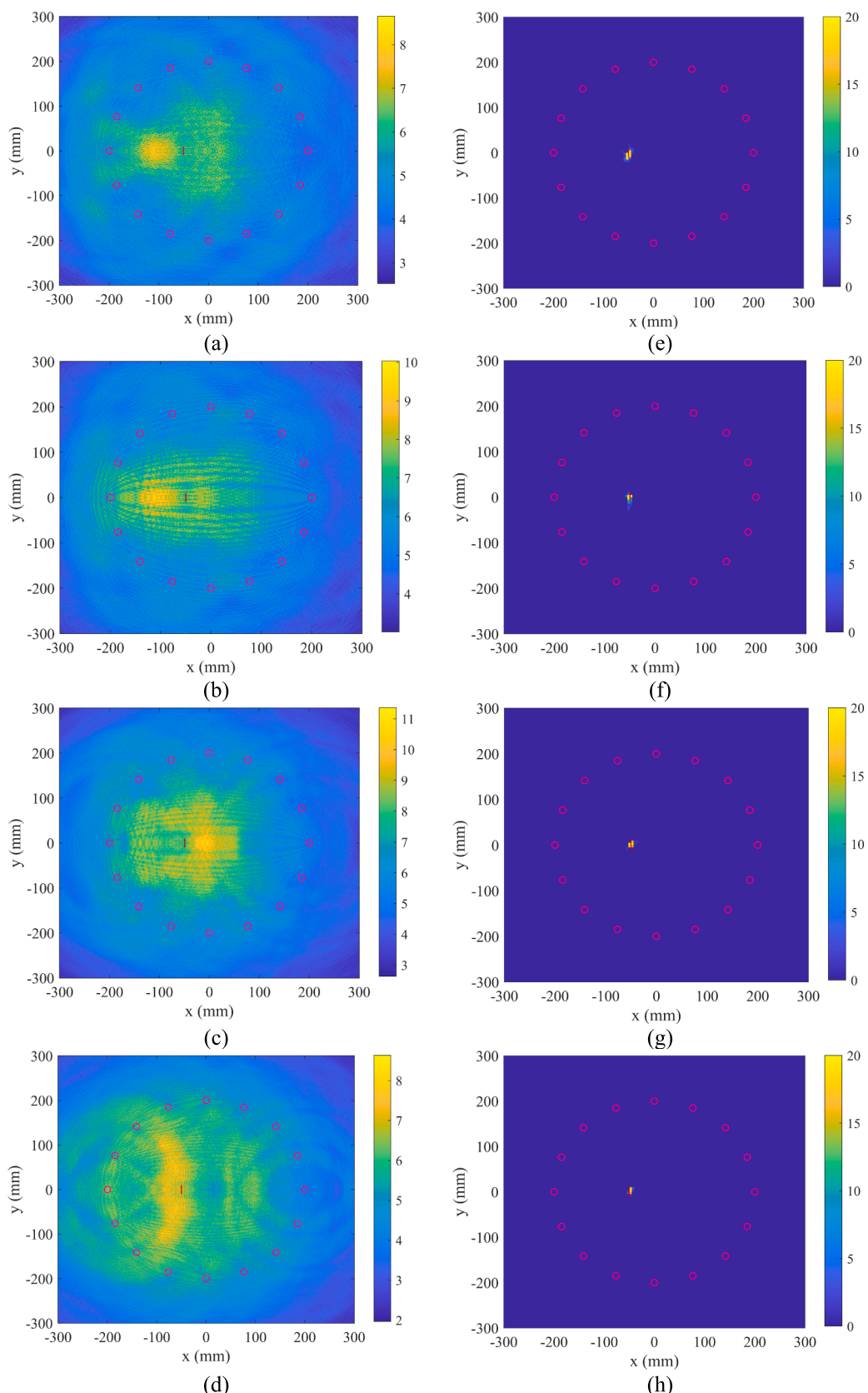


**Fig. 14.** Imaging performance of EIM and PSOIIM for cracks with different lengths: (a) EIM imaging result for 5 mm crack, (b) EIM imaging result for 10 mm crack, (c) EIM imaging result for 15 mm crack, (d) EIM imaging result for 20 mm crack, (e) PSOIIM imaging result for 5 mm crack, (f) PSOIIM imaging result for 10 mm crack, (g) PSOIIM imaging result for 15 mm crack, and (h) PSOIIM imaging result for 20 mm crack.

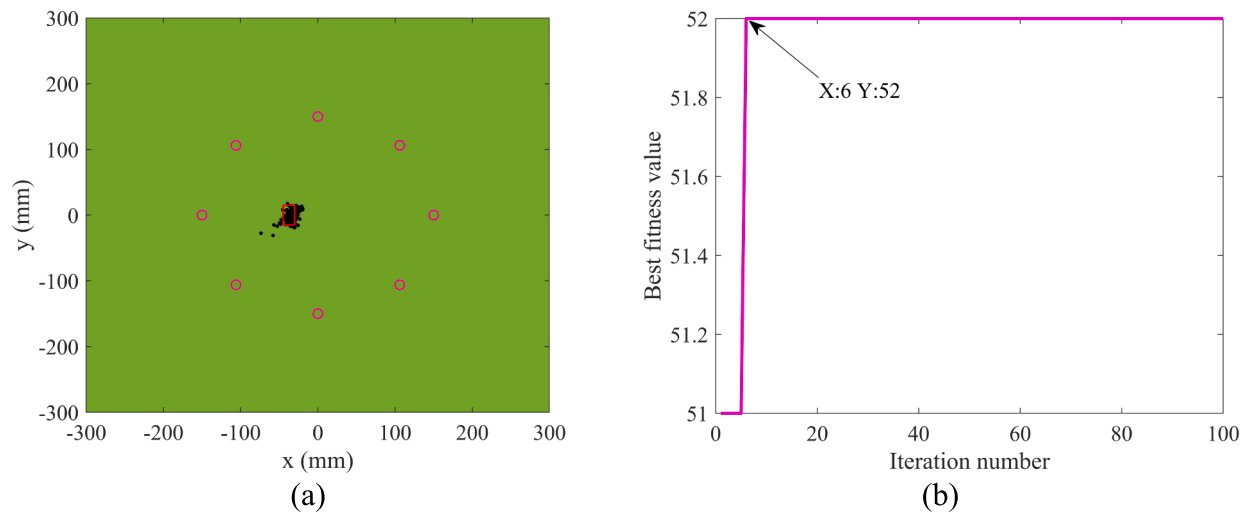


**Fig. 15.** (a) PSOIIM localization result for delamination damage, (b) the convergence curve of the fitness function for PSOIIM to locate delamination damage.

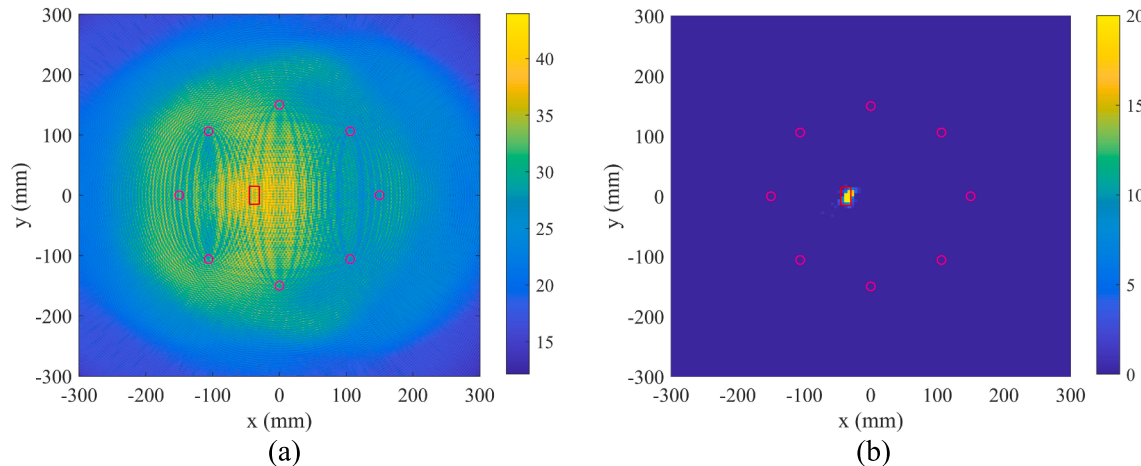


**Fig. 16.** Imaging performance of EIM and PSOIIM for delamination damage: (a) EIM imaging results for delamination damage (b) PSOIIM imaging results for delamination damage.

robustness in locating cracks of different lengths in CFRP structure, and the overall location error is less than 5 mm.

To verify the damage imaging performance of the proposed method, the cracks damage of CFRP structure with different lengths are imaged by the elliptic imaging method (EIM). The discretized detection area in the EIM method has a range of [-300, 300] in the x and y directions, with a resolution of 1 mm. In EIM, VMD is used to denoise the scattering signal, and then the amplitude information of the scattering signal at the ToF of discrete points is extracted for fusion. As shown in Fig. 14(a-d), due to the influence of wave velocity, the imaging spots of 5 mm, 10 mm and 15 mm cracks are located on the left and right sides of the actual damage location respectively. Due to the effect of the number and size of scattering signal wave packets, the imaging spots are much larger than the crack damage. Although the imaging spot of 20 mm crack contains the actual damage location, the transverse effect is obvious and the imaging area is large, so the damage location cannot be accurately identified. The MATLAB function "histogram2" is employed to draw the distribution of population in the specified area. The step size is fixed to 5 mm in x and y orientations. The dynamic range in the bivariate histogram is set between 0 and 20. The imaging results of PSOIIM for 5–20 mm crack damage are displayed in Fig. 14(e-h). The imaging results of PSOIIM can accurately identify the cracks damage location with different lengths, the imaging spots are relatively concentrated and no artifacts are generated.

#### 3.4. Case B: Delamination damage detection

In this section, the application performance of the proposed method for delamination damage detection is evaluated. The parameters of PSOIIM initialization are consistent with the crack detection experiment. The connection diagram of delamination detection experiment is shown in Fig. 4(a). The experimental result of PSOIIM in locating the delamination damage of CFRP is illustrated in Fig. 15(a). After iteration, individuals are basically converged to the delamination damage position. The convergence curve of fitness function for PSOIIM to locate delamination damage of CFRP is presented in Fig. 15(b). The results show that the delamination damage location is searched by some of the best individuals in the 6th generation, and other individuals are converged to the best individual location in the subsequent iteration process. The maximum number of imaging trajectories through the damage location is 52.

The imaging performance comparison of EIM and PSOIIM for delamination damage in CFRP is shown in Fig. 16. The EIM imaging result shows that the delamination damage location is included in the imaging area, but it is difficult to accurately identify the delamination damage location because of the large imaging area caused by the amplitude size and number of wave packets and the transverse effect. The population distribution of PSOIIM for locating delamination damage is plotted using MATLAB function "histogram2". The setting of step

size and dynamic range in the binary histogram are consistent with the crack detection experiment. The PSOIM imaging result shows that the imaging area is matched with the delamination damage, and the location of the delamination damage can be accurately identified.

The complete damage detection analysis of this method is run on a PC with 64 GB RAM and 11th Gen Intel(R) Core (TM) i7-11700 2.50 GHz. The time of crack detection and delamination detection by this method is 82 s and 53 s respectively, which are within the acceptable range in terms of computational efficiency.

#### 4. Conclusions

To improve the damage imaging accuracy of composites structure, an intelligent colony optimization imaging method is proposed, which transforms the damage imaging problem into scattering sources search problem. The fitness function of intelligent imaging method is designed according to the principle that multiple imaging trajectories intersect for damage location. Under the search of PSO algorithm, individuals are finally converged to the damage location by comparing fitness function. The VMD denoising method is used to effectively eliminate the noise interference in the process of obtaining the scattering signal time of flight. The guided wave velocities in all directions of the CFRP structure are obtained by polynomial fitting. The results suggest that the guided wave velocities of the anisotropic CFRP structure with the layup direction of [0/90/0.../0] are generally diamond-shaped. The experimental results of crack and delamination damage detection show that the imaging results of the proposed method can accurately display the location of crack damage with different lengths and delamination damage of anisotropic CFRP structure, the imaging spots are relatively concentrated and no artifacts are generated. It has higher imaging positioning accuracy compared with elliptic imaging method, which verifies the effectiveness and superiority of the proposed method. In the following work, the imaging localization of multiple or multiple types of damage in CFRP structure will be studied and realized.

#### Funding:

This work was supported in part by the Guangdong Province Key Research and Development Program under Grant 2020B0404010001, in part by the National Natural Science Foundation of China under Grant 51975220, in part by the Guangdong Outstanding Youth Fund under Grant 2019B151502057.

#### Declaration of Competing Interest

The authors declare that they have no known competing financial interests or personal relationships that could have appeared to influence the work reported in this paper.

#### Data availability

Data will be made available on request.

#### References

- [1] A. Caggiano, L. Nele, Comparison of drilled hole quality evaluation in CFRP/CFRP stacks using optical and ultrasonic non-destructive inspection[J], *Mach. Sci. Technol.* 22 (5) (2018) 865–880.
- [2] F. Khodayar, F. Lopez, C. Ibarra-Castanedo, et al., Optimization of the inspection of large composite materials using robotized line scan thermography[J], *J. Nondestr. Eval.* 36 (2) (2017) 32.
- [3] M. Senthilkumar, T.G. Sreekanth, R.S. Manikanta, Nondestructive health monitoring techniques for composite materials: a review[J], *Polym. Polym. Compos.* 29 (5) (2021) 528–540.
- [4] C. Xu, Z. Yang, S. Tian, X. Chen, Lamb wave inspection for composite laminates using a combined method of sparse reconstruction and delay-and-sum[J], *Compos. Struct.* 223 (2019) 110973.
- [5] M. Black, S. Kishore, J. LeBlanc, P. Lockhart, A. Shukla, Non-destructive imaging and residual strength of composite materials after exposure to blast loading[J], *J. Dynam. Behav. Mater.* 4 (3) (2018) 408–424.
- [6] T. Gao, X. Liu, J. Zhu, et al., Multi-frequency localized wave energy for delamination identification using laser ultrasonic guided wave[J], *Ultrasonics* 116 (2021), 106486.
- [7] H. Zuo, Z. Yang, C. Xu, et al., Damage identification for plate-like structures using ultrasonic guided wave based on improved MUSIC method[J], *Compos. Struct.* 203 (2018) 164–171.
- [8] B. Zhang, D. Yang, X. Hong, et al., Deep emulational semi-supervised knowledge probability imaging method for plate structural health monitoring using guided waves[J], *Eng. Comput.* (2022) 1–16.
- [9] B. Zhang, X. Hong, Y. Liu, Distribution adaptation deep transfer learning method for cross-structure health monitoring using guided waves[J], *Struct. Health Monit.* (2021), 14759217211010709.
- [10] X. Hong, B. Zhang, Y. Liu, et al., Deep-learning-based guided wave detection for liquid-level state in porcelain bushing type terminal[J], *Struct. Control Health Monit.* 28 (1) (2021) e2651.
- [11] X. Hong, Y. Liu, X. Lin, et al., Nonlinear ultrasonic detection method for delamination damage of lined anti-corrosion pipes using PZT transducers[J], *Appl. Sci.* 8 (11) (2018) 2240.
- [12] X. Hong, Y. Liu, Y. Liufu, et al., Debonding detection in hidden frame supported glass curtain walls using the nonlinear ultrasonic modulation method with piezoceramic transducers[J], *Sensors* 18 (7) (2018) 2094.
- [13] C. Xu, Z. Yang, S. Tian, et al., Lamb wave inspection for composite laminates using a combined method of sparse reconstruction and delay-and-sum[J], *Compos. Struct.* 223 (2019), 110973.
- [14] L. Qiu, M. Liu, X. Qing, et al., A quantitative multidamage monitoring method for large-scale complex composite[J], *Struct. Health Monit.* 12 (3) (2013) 183–196.
- [15] Y. Ren, L. Qiu, S. Yuan, et al., Gaussian mixture model and delay-and-sum based 4D imaging of damage in aircraft composite structures under time-varying conditions [J], *Mech. Syst. Sig. Process.* 135 (2020), 106390.
- [16] G. Liu, Y. Xiao, H. Zhang, et al., Elliptical ring distribution probability-based damage imaging method for complex aircraft structures[J], *J. Vibroeng.* 19 (7) (2017) 4936–4952.
- [17] B. Zima, M. Rucka, Guided waves for monitoring of plate structures with linear cracks of variable length[J], *Arch. Civil Mech. Eng.* 16 (3) (2016) 387–396.
- [18] Y. Liu, X. Hong, B. Zhang, A novel velocity anisotropy probability imaging method using ultrasonic guided waves for composite plates[J], *Measurement* 166 (2020), 108087.
- [19] T. Dokeroğlu, E. Sevinc, T. Kücükylimaz, et al., A survey on new generation metaheuristic algorithms[J], *Comput. Ind. Eng.* 137 (2019), 106040.
- [20] S. Shoa, V. Berbyuk, S. Mustapha, Design optimization of transducer arrays for uniform distribution of guided wave energy in arbitrarily shaped domains[J], *Ultrasonics* 103 (2020), 106079.
- [21] T. Zhang, W. Zhang, X.L. Shao, et al., Research on optimization sparse method for capacitive micromachined ultrasonic transducer array: heuristic algorithm[J], *Sens. Rev.* (2021).
- [22] E. Roux, A. Ramalli, P. Tortoli, et al., 2-D ultrasound sparse arrays multidepth radiation optimization using simulated annealing and spiral-array inspired energy functions[J], *IEEE Trans. Ultrason. Ferroelectr. Freq. Control* 63 (12) (2016) 2138–2149.
- [23] J. Lu, J. Yue, L. Zhu, et al., An improved variational mode decomposition method based on the optimization of salp swarm algorithm used for denoising of natural gas pipeline leakage signal[J], *Measurement* 185 (2021), 110107.
- [24] D. Wang, L. Zhu, J. Yue, et al., Application of improved variational mode decomposition method based on two-dimensional sparrow search algorithm in natural gas pipeline leakage signal denoising[J], 01423312211063688, *Trans. Inst. Meas. Control* (2021).
- [25] M.S. Salmanpour, Z. Sharif Khodaei, M.H. Aliabadi, Transducer placement optimisation scheme for a delay and sum damage detection algorithm[J], *Struct. Control Health Monit.* 24 (4) (2017) e1898.
- [26] H. Chen, Z. Liu, B. Wu, et al., An intelligent algorithm based on evolutionary strategy and clustering algorithm for Lamb wave defect location[J], *Struct. Health Monit.* 20 (4) (2021) 2088–2109.
- [27] Y.S. Andhale, F. Masurkar, N. Yelve, Localization of damages in plain and riveted aluminium specimens using lamb waves[J], *Int. J. Acoust. Vibr.* 24 (1) (2019).
- [28] G.F. Gomes, F.A. de Almeida, D.M. Junqueira, et al., Optimized damage identification in CFRP plates by reduced mode shapes and GA-ANN methods[J], *Eng. Struct.* 181 (2019) 111–123.
- [29] G. Yan, L.L. Zhou, F.G. Yuan, Wavelet-based built-in damage detection and identification for composites[C]//Smart structures and materials 2005: sensors and smart structures technologies for civil, mechanical, and aerospace systems, *Int. Soc. Optics Photon.* 5765 (2005) 324–334.
- [30] P. Bocchini, A. Marzani, E. Viola, Graphical user interface for guided acoustic waves[J], *J. Comput. Civ. Eng.* 25 (3) (2011) 202–210.
- [31] J. Lu, J. Yue, L. Zhu, et al., Variational mode decomposition denoising combined with improved Bhattacharyya distance[J], *Measurement* 151 (2020), 107283.